Chemical Engineering Journal 498 (2024) 153276

Contents lists available at ScienceDirect

Chemical Engineering Journal

journal homepage: www.elsevier.com/locate/cej

Antibubble column: A mean to measure and enhance liquid–gas mass transfer through surfactant-laden interfaces

Jonas Miguet [a,*], Stéphane Dorbolo [b], Benoit Scheid [a]

[a] TIPs, Université Libre de Bruxelles, Brussels, Belgium
[b] PtYX, Soft Matter Pole, CESAM, Université de Liège, Liège, Belgium

ARTICLE INFO

Keywords:
Antibubbles
Mass transfer
Surfactants
Bubble column
Multiphase reactors

ABSTRACT

Antibubbles are ephemeral objects composed of a liquid core encapsulated by a thin gas shell immersed in a liquid bulk. The gas shell thickness evolves in time, driven by two contributions: gravitational drainage and gas–liquid mass transfer. The low density contrast between the antibubble and the bulk, as well as its weak deformability constitute advantages that are used to measure the mass transfer coefficient (MTC) in a so-called antibubble column, in a time-resolved fashion. Shells made with pure air give low data reproducibility. Consequently, perfluorohexane, a low-solubility gas, was mixed to air to enforce gas desorption from the bulk and obtain reliable data. MTC obtained with various surfactants and concentrations are found to deviate from the Frössling correlation built for fully rigid interfaces: higher MTC are consistent with partially rigid interfaces due to a partial coverage of surfactants along a so-called spherical cap, while lower MTC are consistent with an additional resistance to the transfer of mass due to the presence of surfactants forming a monolayer at high concentration. Finally, the advantages in terms of control and compactness of an antibubble column as compared to a bubble column for liquid–gas mass transfer are demonstrated. Specifically, an antibubble is shown to transfer dozens of times more mass than a bubble that would initially carry the same amount of gas. Antibubbles are therefore shown to provide a new, time-resolved, way to measure MTC, as well as promising route to enhance liquid–gas transfers in multiphase reactors.

1. Introduction

The transfer of mass between gas elements and a moving fluid has been thoroughly studied, because of its high applicability in processes involving multi-phase reactors like in chemical, biochemical, petrochemical and pharmaceutical industries [1,2]. From an analytical standpoint, the process is highly complex due to the interplay between gas uptake, chemical reactions, bubble dynamics and flow regimes [3,4]. These technological impact and complexity explain the still very abundant research and development activities in the field [5,6]. A crucial parameter for the quantification of the transfers is the mass transfer coefficient (MTC), usually noted k ($\mathrm{m\,s^{-1}}$).

This parameter is also involved in other technologically and fundamentally relevant systems, such as foams [7,8], as it mediates the coarsening that limits the foam lifetime. At the scale of a film, as an elementary component of a foam, the crucial role of phase change, such as evaporation, on the overall film thinning has also been established [9,10]. In particular, the thinning rate of surface bubbles is more than an order of magnitude lower when the relative humidity is maximized [10]. In addition, it has recently been suggested that the thinning rate could also be linked to the influence of surfactants on k [11], a link that will be confirmed in the present paper. Indeed, because of the difficulty to control the cleanness of a bubble column over time and to quantify the amount of surfactants adsorbed on bubble's surfaces [12], the impact of surfactants is a relevant research topic [13].

Owing to the complexity of the system, numerous correlations have been proposed between the gas uptake [1], which is the volume fraction of gas in an operating bubble column, or mass transfer coefficient [14], and operating conditions. Even in the context of fundamental research, only relatively old experiments exist and suffer from strong limitations, such as bubble dissolution methods [15] that do not account for the inhomogeneity of the thin film thickness, or evaporation resistivity (k^{-1}) measurements [16] that are more qualitative than quantitative. Bubble columns have been recently used to evaluate the impact of surfactants on k, but only one position in the column was probed [17]. Worth mentioning, other experimental configurations like in bamboo-like bubble assemblies [18] or thin film displacement in a syringe [19] have been proposed to sound the influence of surfactants on the MTC.

* Corresponding author.
E-mail address: jonas.miguet@u-paris.fr (J. Miguet).

https://doi.org/10.1016/j.cej.2024.153276
Received 22 April 2024; Received in revised form 13 June 2024; Accepted 17 June 2024
Available online 9 July 2024

Nomenclature

Roman letters

c	Geometrical prefactor of Frössling's correlation, –
c	bulk concentration of surfactant
C	Dissolved gas concentration, mol m^{-3}
C_∞	Dissolved gas concentration far from the antibubble, mol m^{-3}
C_{sat}	Dissolved gas concentration at the outer surface of the antibubble, mol m^{-3}
cmc	Critical micelle concentration, mol
C_D	Drag coefficient, –
D	Diffusion coefficient of dissolved gasses in the liquid, m^2 s^{-1}
g	Gravitational acceleration, m s^{-2}
h	Averaged gas film thickness, m
h_0	Initial averaged gas film thickness, m
h_{min}	Minimal gas film thickness, m
J	Mass flux kg s^{-1}
k	Liquid-side MTC, m s^{-1}
k_{exp}	Experimental MTC, m s^{-1}
$k_{Frössling}$	Frössling's correlation for the MTC, m s^{-1}
k_{Higbie}	Higbie's correlation for the MTC, m s^{-1}
k_{ML}	Monolayer MTC, m s^{-1}
k_{tot}	Total MTC, m s^{-1}
K_H	Henry's constant, mol m^{-3} Pa^{-1}
$\mathcal{L}$	Column height, m
n	Molar quantity of air in the thin film, mol
P	Partial pressure, Pa
P_{atm}	Atmospheric pressure, Pa
P_g	Total gas pressure in the thin film, Pa
r	Size ratio between equivalent bubble and antibubble, –
R	Radius of the antibubbles, m
R_b	Radius of the bubble, m
$\mathcal{R}$	Perfect gas constant, J K^{-1} mol^{-1}
t	Time, s
T	Temperature, K
U	Ascension velocity of the antibubble, m s^{-1}
V_{gas}	Gas film volume, m^3
z	Vertical position of the antibubble, m

Dimensionless numbers

Bo	Bond number, –
Ga	Galileo number, –
Pe	Péclet number, –
Re	Reynolds number, –

Greeks letters

β	Saturation parameter, –
Δ	Difference, –
η	Dynamic viscosity, kg m^{-1} s^{-1}
γ	Surface tension, N m^{-1}
ν	Kinematic viscosity, m^2 s^{-1}
ρ_{AB}	Effective density of the antibubble, kg m^{-3}
ρ_l	Density of the liquid phase, kg m^{-3}
τ	Residence time in the column, s

Subscripts

air	Atmospheric gasses
C_6F_{14}	Perfluorohexane
eq	Equivalent bubble
l	Liquid phase
N_2	Dinitrogen
O_2	Dioxygen

They have demonstrated that the permeability of a liquid membrane to air was correlated to the concentration of adsorbed fluorinated gas molecules on the membrane.

In this paper, we study the transfer of mass between a liquid column and an *antibubble*, named after Pavlov-Verevkin [20], which is a spherical thin shell of gas, surrounded by liquid (see Ref. [21] and references therein). A picture of an antibubble is shown in Fig. 1a, backlighted with a collimated monochromatic lamp. The black corona around the sphere is the signature of the presence of a gas film that implies a total internal reflection [22,23]. The presence of interference fringes shows that the film is of micrometer dimensions and the tightening of the fringes at the top indicates a thicker film there than at the bottom of the antibubble. Antibubbles indeed experience gravitational drainage, because hydrostatic pressure is higher at the bottom than at the top. In addition, the thinning can either be promoted by gas dissolution into the surrounding liquid [24], or delayed by liquid evaporation into the gas film, as we have recently shown in Ref. [25]. Now, in absence of evaporation, the desorption of dissolved atmospheric gases from the oversaturated liquid towards the gas film can also be a mean to counteract gravitational drainage and measure the mass transfer coefficient as detailed in the following.

To address gas–liquid mass transfer in antibubbles, the saturation parameter of dissolved gas in the liquid $\beta = C_\infty/C_{sat}$ is defined, where C_∞ is the molar concentration of dissolved atmospheric gases in the liquid far away from the antibubble, and C_{sat} is the saturation concentration at the antibubble interfaces. Both concentrations are related to Henry's equilibrium [27] that establishes the relationship between the partial pressure P in the gas phase and the dissolved gas concentration C in the liquid phase, namely $C = K_H P$, with K_H the Henry's constant. A typical atmospheric pressure variation during the day in Brussels is about 5 mbar [28], i.e. ±0.25% around a central value. The temperature variations in the lab also affect the Henry's coefficient. Assuming a ±1 °C variation around a central value during the day, the solubility of the gas can change by about ±1.5% (see correlations in [29]). Estimating a typical value for the variations of β would require to consider the dynamics of these environmental changes and how the volume of liquid in which the antibubbles are created dynamically recovers its equilibrium. We assume for illustration purpose that β may depart from unity, *i.e.* full saturation at equilibrium, because of environmental changes by ±1%. Fig. 2 presents the minimum film thickness h_{min} at the bottom of the antibubble, using the model presented in Vitry et al. [26]. This model describes the thinning of an antibubble, driven by hydrostatic pressure difference between the bottom and the top of the antibubble. The Van der Waals contribution destabilizing the film at the nanometric scale was removed for the sake of clarity. The model accounts for the mass transfers through the Epstein–Plesset non-stationary solution for pure diffusion around a sphere [24,30]. The expected $h_{min} \propto t^{-1/2}$ behavior for a rigid, i.e. no-slip, interface is found when β=1. However, when departing from the saturation by only one percent, the thinning dynamics is deeply modified. Controlling the lifetime of antibubbles

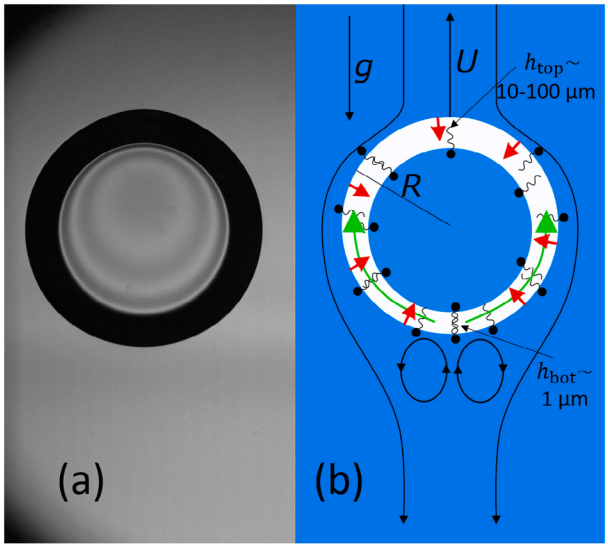

Fig. 1. (a) An antibubble with a radius $R = 4.64$ mm. The antibubble is made neutrally-buoyant with the use of glycerol and therefore lies in an isodense environment [23,26]. (b) Schematic of an antibubble freely ascending in a liquid column at speed U. The drainage of the gas is indicated by the green arrows. If the gas shell is saturated with an insoluble gas, dissolved atmospheric gases are transferred from the surrounding liquid to the shell, as shown by the red arrows. During the ascension, surfactants may be swept towards the rear of the antibubble. Since the Reynolds number is typically around 100, vortices are expected in the wake of the antibubble. Typical thicknesses for the top and bottom parts of the thin film are given based on [23,26]. The thickness of the film is exaggerated in this scheme.

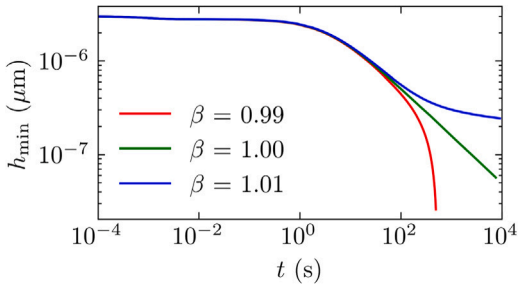

Fig. 2. Temporal evolution of the minimum film thickness h_{min} at the bottom of an antibubble as derived from the numerical model published in Ref. [26], with an antibubble radius $R = 4.64$ mm, an initial thickness $h_0 = 3$ µm, an elasticity of 1 mN m^{-1} and a varying saturation parameter of dissolved gas in the surrounding liquid β.

may therefore come down to controlling the mass exchanges across the interfaces.

In this paper, we find inspiration in the bubble world that came up with bubble columns and conceive an antibubble column. We first show that this configuration allows for the time-resolved determination of the MTC and provide new data for different surfactants at varying concentrations (c). Then, we compare the amount of mass that is exchanged by the antibubble to a bubble that would carry the same initial amount of gas. The results show that the antibubble column may be used with benefit for the design of multiphase reactors.

Compared to the bubble column, the antibubble column presents unique properties that can be used advantageously. The ratio $(\rho_l - \rho_{AB})/\rho_l$, where ρ_l and ρ_{AB} are the density of the liquid and that of the antibubble, respectively, that drives the rising motion, is about $3h/R$ in the limit of $h \ll R$ [26], where h is the averaged gas film thickness and R the radius of the antibubble. The driving force is therefore small and so is the rising velocity U, of the order of 1 cm s^{-1}, which is typically one order of magnitude smaller than for rising bubbles (see Ref. [31] for example). As a consequence, the lower Reynolds number allows for a straight flow path and the Laplace pressure in the incompressible core ensures a nearly spherical shape of the object, which greatly simplifies the observations.

2. Experimental methods

In order to quantify gas–liquid mass transfer coefficient with antibubbles, we designed an original experiment that we call antibubble column (Fig. 3). A $12 \times 12 \times 67$ cm^3 column, filled with the solution of interest is used as a test vessel. A fluorescent tube is placed behind the column with respect to a camera, and tracing paper is used as diffuser to get a more homogeneous enlightenment along the path of antibubbles. A Nikon D3100 camera, combined with a Nikkor AF-S 18–55 mm lens and a timer remote (Phottix TR-90), are used to take pictures at one frame per second during the rise of the antibubble. In our particular enlightment conditions, an F number of 11, an exposure time of 250 µs and an ISO of 6400 allowed for a proper determination of the position and size of the antibubbles. The larger dimension of the 3072 × 4608 pixels CMOS sensor is used for the vertical imaging of the system, with a resolution of about 100 µm/pixels. The production of antibubbles relies on the immersed bell set-up [26,32], represented in figure schematized in Fig. 1c: a bell, with outer dimensions of $12 \times 12 \times 45$ mm^3, with its aperture facing downwards, slightly tilted to avoid collision, is connected to a pressure controller. In our case, the bell is made of a disposable cuvette for spectroscopy, to which holes were pierced in order to glue the proper ports for fluidic connections. One hole is used with an M6 dimension female port for the liquid input of the injector, the other with an M4 female port connection to control the amount of gas in the chamber. The connection of the gas phase in the bell to the pressure controller indeed allows for a fine control of the distance between the liquid level in the bell and the injector, necessary for an optimized production of antibubbles. It also allows to control the nature of the gas in the bell that will constitute the thin film of gas. The injector consists of a 1.57 mm external diameter fluoropolymer tube, plunged inside the bell and sealed with an appropriate nut/ferrule system. This tube is directly inserted into another tube of inner diameter 1.6 mm and waterproofed with a PTFE tape. Once the column is filled with the solution of interest, the pressure in adjusted inside the bell, typically with values around the hydrostatic pressure, i.e. 50 mbar, using a Fluigent MFCZ pressure controller, so that a proper gaz pocket is built up. Then, the tube containing the injected solution, the same as the host one, is pressurized (usually a few hundreds of millibars), with the same multichannel pressure controller. A microfluidic solenoid valve (2-Switch, Fluigent), controlled with a Python script, can then be opened for a fixed amount of time, between 50 and 200 ms, to proceed to the formation of a jet at the tip of the injector.[1] In these conditions the injection time affects the size of the antibubble: longer opening time corresponds to larger antibubbles. The maximum size is nevertheless limited: if the opening time is too long, several antibubbles are generated, which can be advantageous but not considered here. The jet is directed to the liquid surface where it penetrates through the interface, coated with a thin layer of air. This jet then undergoes a Rayleigh–Plateau destabilization [33,34] that eventually leads to the formation of a pocket of liquid surrounded by a thin film of air that rapidly adopts a spherical shape to minimize the surface area: in other words, an antibubble. A sequence of snapshots representing the process is given in Appendix A and in figure 7 of Vitry et al. [26].

Three different surfactants were used to prepare the solutions. A commercial dishwashing liquid (Dreft) was used to assess the behavior of the system, because it is cheap and robustly allows to produce antibubbles. More specifically, Dreft is principally a mixture of sodium

[1] Note that a proper control of the opening time is only achievable with Python version 3.11 and beyond.

Table 1
Surface tension above the cmc and cmc of the surfactant systems used. In the case of Dreft, the cmc is defined as the concentration above which the surface concentration is constant. Data obtained on the basis of a surface tension isotherm obtained by pendent drop measurements.

	Dreft	C_{16}TAB	PS 80
γ (mN m^{-1})	25	38 [35]	43 [36]
cmc	~0.1%	0.92 mM	0.012 mM

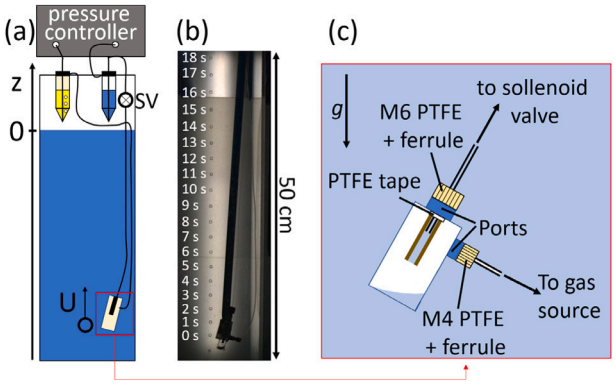

Fig. 3. (a) Experimental set-up for the antibubble column using C_6F_{14}-saturated air. 'SV' refers to the sollenoid valve that controls the opening time, between 50 and 200 ms, of the pressurized surfactant liquid reservoir towards the injector, in order to create antibubbles. (b) Superimposed stack of images representing the ascension of an antibubble in PS80 at 100 cmc. (c) Zoom of the reversed-bell set up [26,32].

lauryl ether sulfate (10–20%), an anionic surfactant and lauryldimethylamine oxide (1–5%), a zwiterrionic one. Better-controlled surfactant systems were used, namely hexadecyltrimethylammonium bromide (Merck, H5882) and polysorbate 80 (Merck, P1754), thereafter referred to, respectively, as C_{16}TAB and PS80. C_{16}TAB is a commonly used cationic surfactant with a 16-carbons long hydrophobic alkyl chain and a critical micelle concentration (cmc) of 0.92 mM. Polysorbate 80 is a non-ionic surfactant with a 18-carbons long aliphatic chain attached to polyethers that provide some affinity with water. Some properties of the different surfactant used for this study are provided in Table 1. The concentrations are chosen so that antibubbles can be produced. Indeed, whether antibubbles can be made or not for a given physical-chemistry is not well understood and assessed here empirically.

Once the antibubble is formed, its vertical path within the column is recorded and the images are processed with the Scikit-image library in Python to get the size and the position as a function of time, from which the ascending velocity is calculated as

$$U = \frac{z_{i+1} - z_i}{\Delta t}\,, \tag{1}$$

where z_i is the vertical position on frame number i and Δt is the time between 2 successive frames (1 s). Fig. 3b represents superimposed images along the vertical ascent of an antibubble. Fig. 4a presents the recorded velocities for antibubbles made with air and Dreft at four different concentrations. This corresponds to the configuration represented on Fig. 3a, but where the vial connected to the bell gas phase does not contain any liquid: only filtered ambient air is used. In this case the data are not satisfactorily reproducible, because, as explained above, the system is extremely sensitive to the value of the saturation parameter β, which is hard to control within less than 1 % (detailed calculation are presented in Appendix B). We indeed observe different speeds and, more importantly, different accelerations, for equivalent radii when only air is used. Therefore, in order to obtain reproducible accelerations, it was necessary to force a concentration gradient between the liquid column and the thin film.

The easiest way to do this in our configuration was to lower the vapor pressure of air within the thin film, by adding another low-solubility gas, namely perfluorohexane C_6F_{14} (Merck, 281042). This compound is liquid but volatile in standard conditions, with a vapor pressure of $P_{C_6F_{14}} = 0.29$ bar [37] and a Henry's coefficient $K_{H,C6}F_{14} = 5.4 \times 10^{-10}$ mol m^{-3} Pa^{-1} [38], which is at least four orders of magnitudes below those of nitrogen and oxygen, respectively, $K_{H,N_2} = 6.4 \times 10^{-6}$ mol m^{-3} Pa^{-1} and $K_{H,O2} = 1.3 \times 10^{-5}$ mol m^{-3} Pa^{-1}. We then allow filtered air to slowly flow through a tube filled with liquid C_6F_{14}, previously left at rest for at least one hour to ensure saturated conditions. The partial pressure of saturated air (treated as a single gas, as emphasized below) is therefore :

$$P_{g,air} = P_{atm} - P_{C_6F_{14}}\,, \tag{2}$$

with $P_{atm} = 1.013$ bar the atmospheric pressure. Hence the volume fraction of air in the film is

$$\alpha \approx \frac{P_{g,air}}{P_{atm}} = \frac{P_{atm} - P_{C_6F_{14}}}{P_{atm}} = 0.705\,, \tag{3}$$

such that the system becomes much less sensitive to any small deviation from equilibrium within the liquid column (see Appendix B). Velocities measured in these conditions actually feature much more reproducible data, as shown in Fig. 4b. We now analyze these data with the aim to quantify the gas transfer and discuss the parameters that affect the measurements.

3. Derivation of the mass transfer coefficient

A qualitative schematic of the situation of an ascending antibubble is given in Fig. 1b. We identify three contributions to the temporal evolution of the velocity of the antibubble: (i) the volumetric expansion of the gas caused by the decreasing hydrostatic pressure as the antibubble rises in the column, (ii) the dissolved gas transfer between the air film and the surrounding media and (iii) the formation of a steady distribution of surfactants along the outer interface, that can lead to the formation of a so-called stagnant cap [12].

Let us start with the third contribution. This stagnant cap refers to the accumulation of surfactants at the rear of a moving fluid sphere in a liquid which induces a local immobility of the interface, in the reference frame of the sphere. In the case of bubble, the dynamics of formation of this stagnant cap can lead to transient velocities [39], with an initial acceleration, a maximum in the velocity and then a decrease, until the final plateau value. This process is associated with the build-up of the stagnant cap that 'rigidifies' the interface. The final, steady state velocity is typically reached in less than one second for intermediate concentrations. In our case, the concentration is relatively high and the velocity small, as compared to the rising bubbles where transient velocities are observed. We can therefore consider that (i) the stagnant cap is immediately formed and remains in a quasi-steady state, such as any variation of the velocity should be caused by mass transfers and/or volumetric expansion; (ii) the angle of the stagnant cap is large, so that the antibubble rises almost as a rigid sphere, an assumption valid as long as at least two thirds of the sphere is covered by surfactants [40]. The spherical assumption made for the antibubble is verified in Appendix C with a better spatially resolved image.

Additionally, we note that a typical velocity for the thin film drainage is of the order of 100 μm s^{-1} [26], while the ascending velocity of the antibubbles U in the column is of the order of 1 cm s^{-1}. We can define a Péclet number for the mass transfer as $Pe = RU/D$, where D is the diffusion coefficient of the dissolved gas molecules within the liquid, equals to 2×10^{-9} m^2 s^{-1} [41]. We then obtain a typical Péclet number of the order of 10^4 for the outer interface of the antibubble. This shows that the convective part is dominant and that the typical velocity at the interface scales with the total mass transfer, which allows us to neglect the transfers across the inner interface of the antibubble.

We want to model the gas content of the antibubble as a function of its ascension velocity. In the spirit of Vitry et al. [26], we first seek a relation between the averaged film thickness h and the ascension

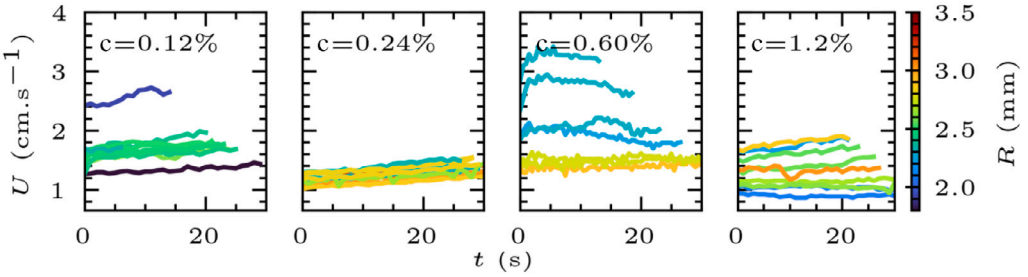

(a) Air-containing antibubbles.

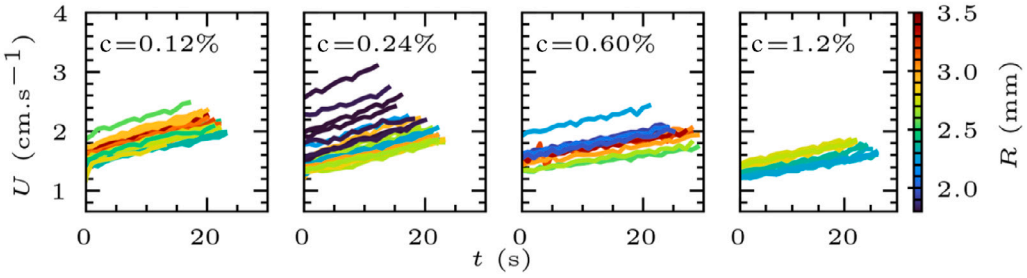

(b) (Air+C_6F_{14})-containing antibubbles.

Fig. 4. Ascension velocity as a function of time for antibubbles with various concentrations (c) of Dreft. The color code scales for the antibubble radius.

velocity U. Balancing buoyancy and drag, and using the fact that $h \ll R$, it reads

$$h = \frac{C_D U^2}{8g}, \tag{4}$$

where C_D is the drag coefficient, which is a function of the Reynolds number defined as

$$Re = \frac{2R\rho_l U}{\eta_l},$$

where $\rho_l = 997\,\mathrm{kg\,m^{-3}}$ is the liquid density and $\eta_l = 0.89\times10^{-3}\,\mathrm{kg\,m^{-1}\,s^{-1}}$ the liquid viscosity. The measured Reynolds number for all experiments analyzed in the paper lies within $60 \le Re \le 220$. For deriving an analytical approximation to describe the system, we build a subset correlation of the more general one given by Brown et al. [42], valid in this range of Reynolds number, and which reads

$$C_D \approx 8.717 Re^{-9/20}, \tag{5}$$

with a root-mean-square-error of 0.018 and a maximum relative error of 2.4%. Plugging (5) into (4) yields

$$h(t) \approx 0.798 \left(\frac{\eta_l}{\rho_l R}\right)^{9/20} \frac{U(t)^{31/20}}{g}. \tag{6}$$

Using now the ideal gas law and still assuming $h \ll R$ for approximating the volume of gas as $V(t) \approx 4\pi R^2 h(t)$, we can write

$$n(t) \approx \frac{4\pi R^2 h(t) P_g(t)}{\mathcal{R}T}, \tag{7}$$

where n is the total number of moles of gas, T=298 K the ambient temperature, $\mathcal{R}$ the gas constant, and P_g the total gas pressure. Taking the origin of the vertical axis, pointing upwards, at the surface of the liquid column (Fig. 3a), the pressure in the gas film is

$$P_g(t) \approx P_{atm} - \rho_l g z(t), \tag{8}$$

with $z(t)$ the position of the antibubble in the column, and where we have neglected the contribution of the Laplace pressure. By adapting the Fick's law with a liquid-side limited transfer, the molar flux may be written [43,44]:

$$\frac{dn}{dt} = 4\pi R^2 k\, K_H(\beta P_{atm} - \alpha P_g), \tag{9}$$

where k ($\mathrm{m\,s^{-1}}$) is the mass transfer coefficient. The saturation parameter of the dissolved gases in the liquid is set to $\beta = 1$, even though it may slightly deviate from unity depending of the variations of temperature, pressure or humidity in the lab. Similarly to [18], we treat air as a single compound with an effective Henry's coefficient $K_H = \frac{P_{N_2}}{P_{atm}} K_{h,N_2} + \frac{P_O}{P_{atm}} K_{h,O_2} \approx 0.78 K_{h,N_2} + 0.21 K_{h,O_2} = 7.7\times10^{-6}\,\mathrm{mol\,m^{-3}\,Pa^{-1}}$, where P_N and P_{O2} are the partial pressures of dinitrogen and dioxygen, respectively. The composition of air could be affected by the presence of water vapor, which we neglect since its partial pressure at 25 ° C is about 3.2 kPa [29] *i.e.* 3.1% of the molar gas content. Finally, (9) gives a definition of k, that effectively represents the rate at which mass is transferred. In the context of mass transfer through thin films or monolayers, this coefficient is sometimes referred to as permeability [18,44].

So, we measure $z(t)$, from which we calculate $U(t)$ using (1). We can then deduce $h(t)$ from (6), $n(t)$ and $P_g(t)$ from (7) and (8), and finally $k(t)$ from (9). A simplified modelization (see Appendix B) of the problem allows to estimate the various contributions to the system. It also allows to justify that the expected velocity profiles are almost linearly increasing in time, which is used thereafter.

Quantitatively, the gas transfer between a liquid bulk and a flowing sphere is made by assuming that the limiting contribution to k is the diffusive boundary layer around the sphere. This implies that the hydrodynamics around the moving sphere determines the quantity of the transfer and needs to be described.

In the case of a sphere with mobile interface, *i.e.* stress-free, Higbie [45] provides a quantitative theory relying on a short contact time and fast liquid renewal between an element of liquid and the sphere's interface where the transfer takes place. His prediction writes

$$k_{Higbie} = \sqrt{\frac{2DU}{\pi R}}. \tag{10}$$

In the case of a sphere with rigid interface, *i.e.* no-slip, Frössling [46] provides a prediction that writes

$$k_{Frössling} = c\sqrt{\frac{U}{2R}} D^{2/3} \nu^{-1/6}, \tag{11}$$

with ν=0.89 × $10^{-6}\,\mathrm{m^2\,s^{-1}}$ the kinematic viscosity of the surrounding liquid and c a constant. The value of this constant is debated [47] but

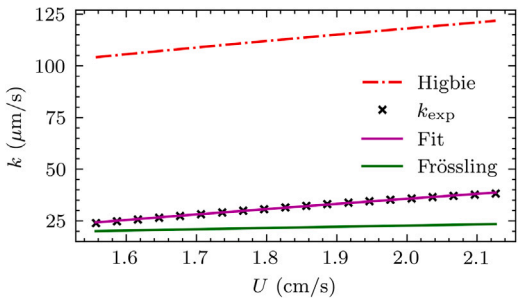

Fig. 5. Experimental mass transfer coefficient (black crosses), as a function of time for a 0.24% Dreft antibubble with R=1.8 mm. The corresponding mass transfer coefficients, based on the measured velocity U, are given for the Frössling (green solid line) and Higbie (red dash-dotted line) correlations. The purple line is the best fit to the experimental data using (12).

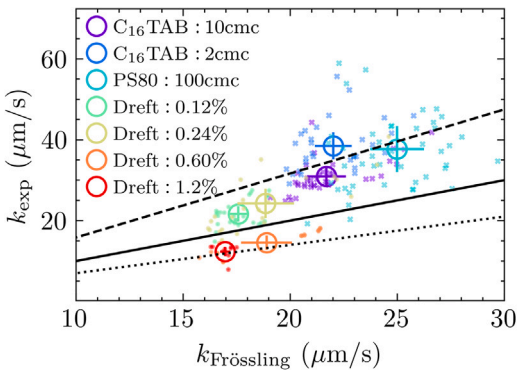

Fig. 6. Experimental mass transfer coefficient as a function of Frössling correlation. The solid line represents (11) with c=0.6, the dashed line with c=0.95 and the dotted line with c=0.42.

we will use c=0.6 as a reference, as reported in [48] for air bubbles in a column and this value is used elsewhere [49,50]. The value of this prefactor is set by the position of the separation point between the boundary layer flow and the wake, and by the proportion of the total flux in both regions [43]. To the best of our knowledge, it has not been derived numerically but Ref. [43] reports experimental values for this constant, ranging from 0.42 [51] (based on the analogy between heat and mass transport around a sphere [52]) to 0.95 [53].

To obtain the value of k from measuring the velocity profile we proceed as follows. After measuring the ascension velocity of a C_6F_{14} saturated antibubble, we obtain experimental profiles that are linearly increasing (see Fig. 4b). To process these data, we fit a linear profile to the experimental one and we deduce the mass transfer coefficient $k(t)$ with the method given above. The first two points of the velocity profiles (first two seconds) are discarded to avoid non-stationary effects at early stages, due to the settlement of the boundary layer and/or the redistribution of the surfactants induced by the flow. The use of a linear form allows to damp the experimental errors due to the weak frequency of acquisition and low spatial resolution. It has no influence on the averaged value of k. A typical result is presented in Fig. 5. From this figure, we see that in this case (Dreft 0.24%), the experimental coefficient falls between that predicted for a rigid sphere (Frössling) and that for a mobile one (Higbie). Also, the evolution in time of the mass transfer coefficient, due to the evolution of the velocity, follows the relationship :

$$k = k_0 + k_1 \left(\frac{U}{R}\right)^{1/2}, \tag{12}$$

where k_0 (m s^{-1}) and k_1 (m s$^{-1/2}$) are constants. This picture is characteristic of the system and is verified for all experiments presented in the paper. The fitting coefficients for all sets of experiments are given in Appendix D. This treatment leads to the following remarks: (i) the initial measured value for k lies above the rigid limit in all cases except for highly concentrated Dreft; (ii) the rate of increase of k as a function of U is between that for the rigid and mobile cases. Finally, since the velocity increases by up to a factor 2, then k changes by up to a factor $\sqrt{2}$ and for the sake of simplicity we can discuss on the averaged values of k and retrieve the same conclusions as the two-parameters fits presented in Appendix D.

4. Results and discussion

The experimental values for k are reported in Fig. 6 as a function of the expected value for a rigid sphere for all the tested solutions. The error bars are ± one standard deviation around the averaged value that is given by thick open circles. The large errors on $k_{\mathrm{Frössling}}$ come from the dispersion of initial velocities, attributable to an initial thickness that is also significantly dispersed [26]. In the context of ascending bubbles, several authors reported intermediate values between Frössling and Higbie correlations [17,48–50,54–56]. The values reported here are much closer to the Frössling correlation than the Higbie one (not shown because about 5 times larger than the Frössling correlation), which is consistent with the use of (6) that relies on a rigid sphere assumption. The reported extremal values for the prefactor c are also used and we see that both higher and lower measurements exist in our dataset, which then requires further discussion. The differences between the averaged values and the expected ones from the rigid case with c=0.6 can be as high as 57% in the case of C_{16}TAB, 2 cmc.

For the PS80, the C16-TAB and the low concentration Dreft experiments, the measured mass transfer coefficient k_{exp} is slightly above the one expected for a rigid sphere. Sadhal & Johnson [57], later confirmed by Cuenot et al. [40] in the context of higher Reynolds numbers, showed that the drag coefficient of the sphere corresponds to that of a rigid sphere for a stagnant cap covering at least two thirds of the bubble surface. We can then get a situation where the global drag coefficient is that of a rigid sphere, but with a portion at the head of the sphere where the boundary condition is locally mobile. This should foster faster liquid renewal near the head of the sphere, hence strengthen local concentration gradients and enhance mass transfer. This picture is consistent with the fact that smaller concentration is associated to higher k in the case of C_{16}TAB.

In the case of highly concentrated Dreft, the mass transfer coefficient falls by 27% and 30% below the Frössling prediction for 0.6% and 1.2%, respectively. In the context of mass transfer through soap films, some authors report a non-negligible resistance of the monolayer of surfactants on the gas transfer. The total mass transfer coefficient may be written, analogously to the conduction of electricity in series circuits as

$$\frac{1}{k_{\mathrm{tot}}} = \frac{1}{k_{\mathrm{ML}}} + \frac{1}{k}, \tag{13}$$

where k is the liquid side mass transfer coefficient and k_{ML} that of the interface covered by a monolayer of surfactants. By using the experimental value for k_{tot} and (11) for k, one finds for k_{ML} 69 and 62 μm s^{-1} for 0.6% and 1.2%, respectively. These values are coherent with reported trends [18] for tetradecyltrimethylammonium bromide and sodium dodecyl sulfate, where this permeability is shown to depend on the partial pressure of C_6F_{14}, suggesting that the interaction with that insoluble gas and the hydrophobic tails is responsible for the damping of the total permeability.

5. Comparison between bubble and antibubble columns

In this work, we use antibubbles for the first time in the context of gas–liquid mass transfer and we therefore quantify in this section the advantages of the antibubble column as compared to the bubble column; a first advantage being the huge area of exchange per unit volume of gas, which is $1/h$ for an antibubble [26], as compared to $3/R_{\mathrm{b}}$ for a bubble of radius R_{b}.

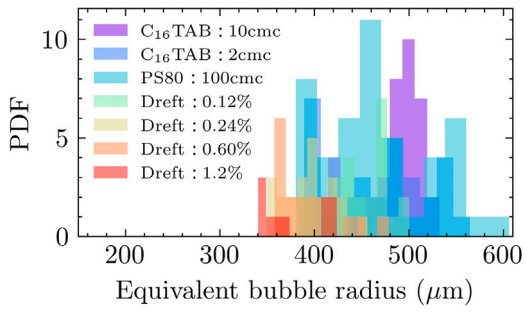

Fig. 7. Size distribution of the equivalent bubble calculated with (15), defined as the bubble that contains the same amount of gas than its antibubble counterpart.

5.1. Comparing contact area

To quantify the performance of an antibubble as compared to an equivalent bubble that would carry the same amount of gas, we first need to compute the total volume of embarked gas in an antibubble at time $t = 0$,

$$V_{\text{gas}} = \frac{4}{3}\pi(R^3 - (R - h_0)^3)\,, \tag{14}$$

where $h_0 = h(0)$ is estimated using (6). The equivalent bubble radius is then

$$R_{\text{eq}} = \left(\frac{3V_{\text{gas}}}{4\pi}\right)^{1/3} = (R^3 - (R - h_0)^3)^{1/3}\,. \tag{15}$$

The distribution of equivalent bubble radii for all the antibubbles measured in this work is given in Fig. 7. Taking the mean value of this distribution gives the average ratio

$$r = \frac{R_{\text{eq}}}{R} \approx 0.19\,. \tag{16}$$

This means that for an equivalent volume of embarked air, a bubble would feature a surface of exchange of approximately r^2, *i.e.* 3.6% of that of an antibubble.

The Bond number $\text{Bo} = \rho_l g(2R_{\text{eq}})^2/\gamma$ with $\gamma \approx 0.04$ mN m^{-1} the surface tension, is 0.2, and the Galileo number $\text{Ga} = \rho_l g^{1/2}(2R_{\text{eq}})^{3/2}/\eta_l$ is 96, meaning that only weak deformations and no path instability is expected for the equivalent bubbles [58]. Additionally, the upper bound for the Reynolds number, based on an overestimated (see below) Stoke's velocity, is about 400. The correlation given by (5) used for the drag coefficient C_D still holds up to $Re = 400$ within 1.5% of root-mean-square error and a maximum error of 3.6%.

Writing the force balance for the rise of the equivalent bubble in stationary state,

$$\frac{4}{3}\pi R_{\text{eq}}^3 \rho_l g = \frac{\pi}{2} C_D \rho_l R_{\text{eq}}^2 U_{\text{eq}}^2, \tag{17}$$

and using (5) for the drag coefficient, yield the equivalent velocity

$$U_{\text{eq}} \approx 0.5695 \left(\frac{g^{20}\rho_l^9 R_{\text{eq}}^{29}}{\eta_l^9}\right)^{1/31}, \tag{18}$$

which is of the order of 10 cm s^{-1} (against 1 cm s^{-1} for antibubbles), hence a Reynolds number of about 100, well below 400.

5.2. Comparing mass transfer

A given amount of mass transferred to or from the antibubble writes

$$\Delta m = J\tau\,, \tag{19}$$

where $J = M\,\mathrm{d}n/\mathrm{d}t$ is the total mass flux with M the molar mass of the transferred species, and

$$\tau = \frac{\mathcal{L}}{U} \tag{20}$$

the residence time in the antibubble column of length $\mathcal{L}$. Using (9) and (11), we get

$$J \propto U^{1/2} R^{3/2}. \tag{21}$$

Equating the amount of transferred species calculated with (19), using (20) and (21), for columns with equivalent bubbles and antibubbles, we can write the ratio of column lengths :

$$\frac{\mathcal{L}_{\text{eq}}}{\mathcal{L}} = \left(\frac{U_{\text{eq}}}{U}\right)^{1/2} \left(\frac{R}{R_{\text{eq}}}\right)^{3/2}. \tag{22}$$

Evaluating U_{eq} from all h_0 reported in Fig. 7 using (18), we find an averaged value of 30 for (22), showing that for the same initial mass of gas, a bubble requires a column 30 times taller than an antibubble.

Alternatively, we can compare the total amount of gas transferred in columns of the same height, *i.e.* $\mathcal{L}_{\text{eq}} = \mathcal{L}$, using again (19), (20) and (21),

$$\frac{J_{\text{eq}}\tau_{\text{eq}}}{J\tau} = \left(\frac{U}{U_{\text{eq}}}\right)^{1/2} \left(\frac{R_{\text{eq}}}{R}\right)^{3/2}. \tag{23}$$

This ratio, calculated for each of the 191 data points, is 3.7% as a mean value.[1] Consequently, an antibubble transfers a much larger amount of mass while traveling in the same column than a bubble that would carry the same amount of gas.

Conclusions above were not trivial at a first glance since several competing effects are at stake. On the one hand, the mass transfer coefficient for equivalent bubbles is higher than for antibubbles because their velocity is greater and their radius smaller (see (11)). On the other hand, equivalent bubbles being faster and smaller, both their residence time and their contact area are smaller than for antibubbles, which at the end makes the difference and explains why the transfer of mass is more efficient for antibubbles, despite their smaller mass transfer coefficient.

5.3. Correction for stress-free equivalent bubbles

While surfactants are absolutely necessary to stabilize antibubbles, they are not necessary for bubbles, which appeals to refine the comparison made above considering bubbles with stress-free interfaces, knowing that they would travel faster than with rigid interfaces and will thus have a still higher mass transfer coefficient (compare (10) and (11)).

We here use the correlation of Mei et al. [59,60] for the drag coefficient of bubbles with stress-free interfaces

$$C_D = \frac{24}{Re}\left(\frac{2}{3} + \left[\frac{12}{Re} + 0.75\left(1 + \frac{3.315}{Re^{1/2}}\right)\right]^{-1}\right), \tag{24}$$

valid for $0 < Re < 1000$. Using then Higbie's mass transfer coefficient (10) to evaluate (19) for the equivalent bubble, the ratio of the total amount of gas transferred in the same column ($\mathcal{L}_{\text{eq}} = \mathcal{L}$) becomes

$$\begin{aligned}\frac{J_{\text{eq}}\tau_{\text{eq}}}{J\tau} &= \frac{k_{\text{Higbie}} R_{\text{eq}}^2 U}{k_{\text{Frössling}} R^2 U_{\text{eq}}} \\ &= \left(\frac{U}{U_{\text{eq}}}\right)^{1/2} \left(\frac{R_{\text{eq}}}{R}\right)^{3/2} \left(\frac{\nu}{D}\right)^{1/6} \frac{2}{c\sqrt{\pi}}\,,\end{aligned} \tag{25}$$

which yields 19.4% based on initial velocities and radius.[2]

We then show that the total mass transferred in a column of the same height is more than 5.2 times larger[3] for a stress-free bubble than

[1] Note that a complete integration accounting also for volume expansion gives 4.1% (not detailed here).

[2] A more rigorous integration (not detailed here), accounting for the velocity and radius evolutions due to both volume expansion and mass transfers yields 12.9% .

[3] Only 3.2 times larger if one accounts for the volume expansion.

for a bubble with a rigid interface; yet, it is still much lower than for an antibubble carrying the same amount of gas, despite a much higher mass transfer coefficient.[4]

Now, the higher velocity of a stress-free equivalent bubble responsible for the higher mass transfer coefficient, also leads to a shorter residence time.[5] As a consequence, the column height for the same amount of transferred mass, based on initial velocity and radius, would be about 50 times larger in the case of an equivalent stress-free bubble than for an antibubble.

6. Conclusion

We propose an original set-up to measure the mass transfer coefficient from a continuous liquid towards a moving fluid sphere. The originality of the system relies on the use of antibubbles that rise much slower than bubbles, which allows to avoid complications such as bubbles deformation or zig-zag instabilities of the ascending object. A simple measure of the ascending velocity provides a measurement for the instantaneous value of k. With the surfactants used, we show that most values fall around that expected for a rigid sphere with differences that are consistent with (i) the existence of an area bare of surfactants at the top of the antibubble, associated with a stress-free boundary condition and a faster local renewal of liquid for the higher values of k, and (ii) with a reduced transfer due to the presence of surfactants, at high concentrations, for the lower values of k. This set-up then constitutes a new measurement tool for the mass transfer coefficient. Additionally, since it turns out that the acceleration of the antibubbles is nearly constant, the size of the column could be reduced even more, while still obtaining reliable data on the transfer. This would allow to decrease the quantity of solution and increase the spatial resolution of the images. Next, by tuning the density of the core solution, slower velocities and therefore smaller k could be measured, which could allow measuring more finely the potential resistance to mass transfer induced by the presence of surfactant monolayers.

Finally, to demonstrate the interest of using an antibubble column in gas–liquid exchange processes, we compare the performance with a column that would contain bubbles carrying an equivalent amount of gas. Overall, for an equivalent column height, bubbles travel approximately 5 times faster than antibubbles and transfer 100 times less mass. For an equivalent amount of transferred mass, a bubble would then require a column 30 times taller than an antibubble; and it would even be 50 times taller in case of a bubbles with stress-free interfaces. A comparison at the scale of a reactor, with a large number of antibubbles, would require an experimental characterization that is beyond the scope of this work. We however emphasize that the amount of surface per unit column volume, that is typically around 10–100 m^2/m^3 in bubble columns [2], is achievable by producing twenty antibubbles per second in a cylindrical column of height 50 cm and radius 10 cm. This is technically feasible with multiple injectors and will be the subject of future works.

Contrarily to our calculations considering gas desorption, if the purpose of the antibubble column would be to dissolve gas, antibubbles may collapse in the process because it gets more fragile as the gas film becomes thinner. This would however result in the creation of numerous tiny bubbles (see for instance [61]) that remain beneficial for the transfer of mass and are hard to make otherwise [62].

Among the transfer-limited chemical reactions that currently involve bubbles are ozonation [63] or microbial electrosynthesis [64].

[4] The ratio of mass transfer coefficients between the equivalent stress-free bubble and the antibubble is 43, while it was 5 in the case of an equivalent rigid bubble.

[5] For instance, the residence time in a 50 cm height column is 22.1 s for an antibubble, 4.79 s for an equivalent rigid bubble and only 1.76 s for an equivalent stress-free bubble.

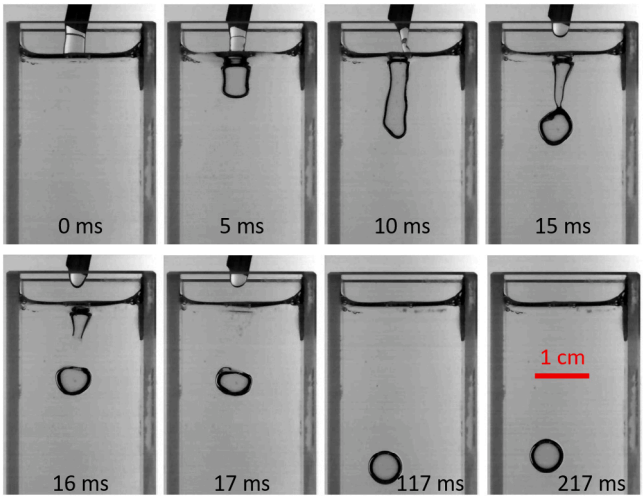

Fig. 8. Snapshots of the manual creation of an antibubble in a 1.2% Dreft solution with a straw.

Worth mentioning finally are, first, the low shear around the antibubble that could be advantageously used in the context of bioreactors involving algae [65], for which high velocity and concomitant high shear are detrimental. And second, the transfer of dissolved gases can also be a mean to control the thinning of the gas film and then control the stability of antibubbles.

CRediT authorship contribution statement

Jonas Miguet: Writing – review & editing, Writing – original draft, Visualization, Methodology, Investigation, Formal analysis, Data curation, Conceptualization. **Stéphane Dorbolo:** Writing – review & editing, Validation, Supervision, Methodology, Investigation, Funding acquisition, Conceptualization. **Benoit Scheid:** Writing – review & editing, Validation, Supervision, Project administration, Methodology, Investigation, Funding acquisition, Formal analysis, Conceptualization.

Declaration of competing interest

The authors declare that they have no known competing financial interests or personal relationships that could have appeared to influence the work reported in this paper. This work has been the subject of a patent application under the number EP24188178.8.

Data availability

Data will be made available on request.

Acknowledgments

We thank Hervé Baudine for his help in the manufacture of the column. We are grateful to Cyril André for providing the surface tension isotherms of Dreft. We thank FNRS for financial support under the PDR-STABAB grant, Belgium. SD and BS are both FNRS researchers.

Appendix A. Antibubble formation

Fig. 8 presents a series of snapshots with a spatio-temporal resolution of 50 μm and 1 ms, respectively. The antibubble is created manually with a straw, following Suhr [23] and provides a good image of the creation of an antibubble from an impacting jet, as is verified in the bell set-up for which this type of series was shown in figure 7 of Vitry et al. [26]. In proper conditions in terms of kinetic to surface energy ratio [34], the jet penetrates through the liquid–gas interface, coated with a gas layer, a process quite similar to the Landau–Levich–Derjaguin phenomenon [26]. This jet is then destabilized in

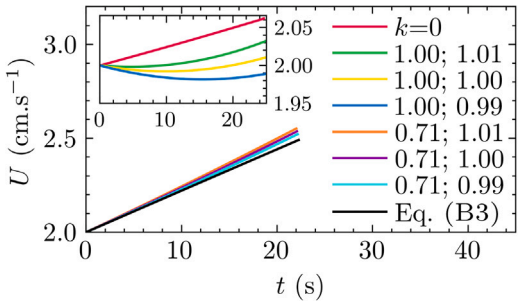

Fig. 9. A simplified model to describe the expected velocity profile for different hypotheses. The values in the legend correspond to (α; β) pairs; $k = 0$ corresponds to the situation where no mass transfer occurs and only the volume expansion contributes to the evolution of the velocity. The black line is the analytical model in which volumetric expansion is neglected.

a Rayleigh–Plateau fashion [34] until the complete pinch-off of the column is achieved, leading to the formation of an antibubble.

Appendix B. Modeling of the system

Deriving the perfect gas law in time, using

$$\frac{\mathrm{d}P_g}{\mathrm{d}t} = -\rho_l g \frac{\mathrm{d}z}{\mathrm{d}t} = -\rho_l g U\,, \tag{B.1}$$

yields

$$\frac{\mathrm{d}h}{\mathrm{d}t} = \frac{\mathcal{R}T}{4\pi R^2}\left(\frac{1}{P_g}\frac{\mathrm{d}n}{\mathrm{d}t} + \frac{n}{P_g^2}\rho_l g U\right). \tag{B.2}$$

By equating the time derivative of (6) with (B.2) combined with (9) and (8), the evolution of the system may be calculated. This relies on the assumption of quasi-steady behavior of the velocity of the antibubble with respect to the mass flux and volumetric expansion. By measuring $U_0 = U(t = 0)$, one can derive $h(t = 0)$ from (6). $P_g(t = 0)$ is derived from the measured altitude $z_0 = z(t = 0)$ and $n(t = 0)$ is deducted from (7). To give an idea of the evolution of the system, we take a constant k=20 μm s^{-1}. This is justified as a first approach by the weak evolution of U and the proportionality of k with $U^{1/2}$. With representative values for $U_0 = 2$ cm s^{-1}, $R = 2$ mm and $z_0 = -50$ cm, Fig. 9 presents the outputs of this simple model for different values of β, defined as the ratio between the saturation concentration of dissolved gases in the column and the actual one. β depends on the atmospheric pressure, temperature, humidity conditions and how quickly equilibrium is met when these parameters are changed. Assuming that this value may change by ±1% around saturation, the inset of Fig. 9 shows that both decreasing and increasing velocities are possible, which explains the lack of reproducibility of the data when only air is used (α=1). On the other hand, in the case of no transfer (k=0), only the volume expansion contributes to the acceleration. The main plot of Fig. 9 represents the same equation system but with C_6F_{14} (α=0.71). The acceleration is much more pronounced in this case and, if the influence of β is still visible, the slope changes by less than 10%.

We can modify the model by assuming that the volume expansion is negligible and by writing $k = aU^{1/2}$, with a a proportionality constant, in agreement with (10) and (11). We then neglect the second term in the right-hand side of (B.2). With the crude assumption that P_g is constant, which reduces to consider that the difference between the film pressure and the partial pressure of air ($\approx 0.3P_g$) is large in front of $\rho_l g z$, that has a maximal value for $z_0 \approx -50$ cm ($\approx 0.05P_g$), we can combine the simplified (B.2) with (6) and find:

$$U \approx \left(0.849\frac{\mathcal{R}T}{P_g}aK_H(P_{atm} - \alpha P_g)\frac{1}{R^{1/20}}\left(\frac{\rho_l}{\eta_l}\right)^{9/20} gt + U_0^{21/20}\right)^{20/21}. \tag{B.3}$$

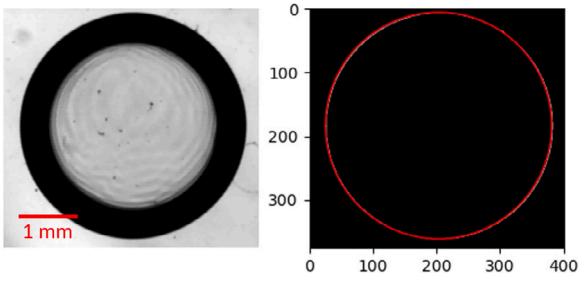

Fig. 10. (a) An antibubble obtained manually with PS80 (100 cmc). (b) Contour plot of (a) with superimposed best fitting circle.

Table 2
Values of fit parameters normalized by the calculated value for the rigid case (Frössling correlation). In the case of the Higbie correlation, both parameters are equal to 5.30. N is the number of antibubbles that were measured in each case and the spread on the experimental data is quantified with ± one standard deviation around the averaged value.

Experiment	N	$\frac{k_0}{k_{\text{Frössling}}(U_0,R)}$	$\frac{k_1\left(\frac{U}{R}\right)^{1/2}}{k_{\text{Frössling}}(U(t),R)}$
C_{16}TAB, 2 cmc	30	1.59 ± 0.24	4.45 ± 0.78
C_{16}TAB, 10 cmc	39	1.34 ± 0.13	3.27 ± 0.57
TW80, 100 cmc	47	1.43 ± 0.36	2.91 ± 1.63
Dreft, 0.12%	27	1.08 ± 0.13	3.42 ± 0.53
Dreft, 0.24%	23	1.09 ± 0.19	3.73 ± 0.82
Dreft, 0.6%	15	0.70 ± 0.08	1.71 ± 0.21
Dreft, 1.2%	10	0.66 ± 0.09	1.94 ± 0.36

This result is consistent with the observations in the sense that the dependency between U and t is nearly linear, as shown in Fig. 9. The associated slowly changing k also justifies *a posteriori* the constant value used for the simplified modelization presented in the beginning of the appendix.

Appendix C. Assessment of the roundness of antibubbles

An assessment of the roundness of antibubbles is performed to ensure that the spherical assumption is valid. Fig. 10a represents an antibubble obtained manually with a diameter of 3.8 mm. This raw image is binarized and the perimeter p and area A of the antibubble are measured using the diplib library in python. The roundness parameter is calculated as $\frac{4\pi A}{p^2}$ and is found robustly superior to 0.995, using different thresholding methods. Given that a perfect circle has a roundness of 1, we can state that the sphericity assumption is validated. The best fitting circle using a Hough transform is also shown on the antibubble after contour detection in Fig. 10b.

Appendix D. Fitting parameters of k from the experimental results

See Table 2.

References

[1] N. Kantarci, F. Borak, K.O. Ulgen, Process Biochem. 40 (2005) 2263.
[2] G. Besagni, F. Inzoli, T. Ziegenhein, ChemEngineering 2 (2018) 13.
[3] M. Martín, M. Galán, R. Cerro, F. Montes, Bubble Sci. Eng. Technol. 3 (2011) 48.
[4] Y. Shah, B.G. Kelkar, S. Godbole, W.-D. Deckwer, AlChE J. 28 (1982) 353.
[5] G. Besagni, Int. J. Multiph. Flow 135 (2021) 103510.
[6] P. Rollbusch, M. Bothe, M. Becker, M. Ludwig, M. Grünewald, M. Schlüter, R. Franke, Chem. Eng. Sci. 126 (2015) 660.
[7] P. Stevenson, Foam Engineering: Fundamentals and Applications, John Wiley & Sons, 2012.
[8] I. Cantat, S. Cohen-Addad, F. Elias, F. Graner, R. Höhler, O. Pitois, F. Rouyer, A. Saint-Jalmes, Foams: Structure and Dynamics, OUP Oxford, 2013.
[9] L. Champougny, J. Miguet, R. Henaff, F. Restagno, F. Boulogne, E. Rio, Langmuir 34 (2018) 3221.
[10] J. Miguet, M. Pasquet, F. Rouyer, Y. Fang, E. Rio, Soft Matter 16 (2020) 1082.

[11] M. Pasquet, F. Boulogne, J. Sant-Anna, F. Restagno, E. Rio, Soft Matter 18 (2022) 4536.
[12] S. Dukhin, V. Kovalchuk, G. Gochev, M. Lotfi, M. Krzan, K. Malysa, R. Miller, Adv. Colloid Interface Sci. 222 (2015) 260.
[13] Q. Liu, J. Zhang, X. Guan, N. Yang, Chem. Eng. J. 455 (2023) 140682.
[14] A.A. Kulkarni, Ind. Eng. Chem. Res. 46 (2007) 2205.
[15] D. Exerowa, D. Kashchiev, D. Platikanov, Adv. Colloid Interface Sci. 40 (1992) 201.
[16] V. Mer, New York/London, 1962, https://www.sciencedirect.com/book/9781483229478/retardation-of-evaporation-by-monolayers.
[17] G. Lebrun, S. Benaissa, C. Le Men, V. Pimienta, G. Hébrard, N. Dietrich, Chem. Eng. Sci. 247 (2022) 117102.
[18] C. Hadji, B. Dollet, H. Bodiguel, W. Drenckhan, B. Coasne, E. Lorenceau, Langmuir 36 (2020) 13236.
[19] B. Dollet, Langmuir 39 (2023) 16174.
[20] B.S. Pavlov-Verevkin., Khimiya i Zhizn' [Chemistry and Life] 11 (1966) 12.
[21] D.N. Sob'yanin, Phys. Rev. Lett. 114 (2015) 104501.
[22] S. Dorbolo, E. Reyssat, N. Vandewalle, D. Quéré, Europhys. Lett. 69 (2005) 966.
[23] W. Suhr, Eur. J. Phys. 33 (2012) 443.
[24] B. Scheid, J. Zawala, S. Dorbolo, Soft Matter 10 (2014) 7096.
[25] J. Miguet, B. Scheid, L. Maquet, B. Darbois-Texier, S. Dorbolo, Phys. Rev. Lett. 131 (2023) 184001.
[26] Y. Vitry, S. Dorbolo, J. Vermant, B. Scheid, Adv. Colloid Interface Sci. 270 (2019) 73.
[27] W. Henry, Philos. Trans. R. Soc. Lond. (1803) 29–274.
[28] Atmosphericpressurebarometer, 2023, https://barometricpressure.app/brussels.
[29] D.W. Green, R.H. Perry, Perry's chemical engineers' handbook, eighth edition, in: McGraw Hill professional, McGraw Hill LLC, ISBN: 9780071593137, 2007, https://books.google.fr/books?id=tH7IVcA-MX0C.
[30] P.S. Epstein, M.S. Plesset, J. Chem. Phys. 18 (1950) 1505.
[31] M. Krzan, J. Zawala, K. Malysa, Colloids Surf. A Physicochem. Eng. Asp. 298 (2007) 42.
[32] B. Scheid, Y. Vitry, S. Dorbolo, Antibubble generator, 2017, European Patent, EP 3 202 491 A1.
[33] S. Dorbolo, H. Caps, N. Vandewalle, New J. Phys. 5 (2003) 161.
[34] P.G. Kim, H. Stone, Europhys. Lett. 83 (2008) 54001.
[35] C. Stubenrauch, V. Fainerman, E. Aksenenko, R. Miller, J. Phys. Chem. B 109 (2005) 1505.
[36] L.S. Wan, P.F. Lee, J. Pharmaceut. Sci. 63 (1974) 136.
[37] G.A. Crowder, Z.L. Taylor, T.M. Reed III, J.A. Young, J. Chem. Eng. Data 12 (1967) 481.
[38] R. Sander, Atmos. Chem. Phys. 15 (2015) 4399.
[39] J. Zawala, J. Miguet, P. Rastogi, O. Atasi, M. Borkowski, B. Scheid, G.G. Fuller, Adv. Colloid Interface Sci. 317 (2023) 102916.
[40] B. Cuenot, J. Magnaudet, B. Spennato, J. Fluid Mech. 339 (1997) 25.
[41] E.L. Cussler, Diffusion: Mass Transfer in Fluid Systems, Cambridge university press, 2009.
[42] P.P. Brown, D.F. Lawle, J. Environ. Eng. 129 (2003) 222.
[43] A. Lochiel, P. Calderbank, Chem. Eng. Sci. 19 (1964) 471.
[44] H. Princen, S. Mason, J. Colloid Sci. 20 (1965) 353.
[45] R. Higbie, Trans. Am. Inst. Chem. Engrs. 31 (1935) 365.
[46] N. Frössling, Gerlands Beiträge zur Geophysik 52 (1938) 170.
[47] W.A. Sirignano, Fluid Dynamics and Transport of Droplets and Sprays, Cambridge university press, 2010.
[48] R. Griffith, Chem. Eng. Sci. 12 (1960) 198.
[49] J.M. Vasconcelos, S.P. Orvalho, S.S. Alves, AIChE J. 48 (2002) 1145.
[50] B. Zhang, Z. Wang, Y. Luo, K. Guo, L. Zheng, C. Liu, Sep. Purif. Technol. 308 (2023) 122888.
[51] Y. Tang, J. Duncan, H. Schweyer, Tech. Rep., Nasa, 1953.
[52] W. Ranz, W. Marshal, J. Chem. Eng. Prog. (1952) 3.
[53] F. Garner, R. Suckling, AIChE J. 4 (1958) 114.
[54] M. Jimenez, N. Dietrich, J.R. Grace, G. Hébrard, Water Res. 58 (2014) 111.
[55] M. Jimenez, N. Dietrich, G. Hébrard, Chem. Eng. Sci. 100 (2013) 160.
[56] W. Nock, S. Heaven, C. Banks, Chem. Eng. Sci. 140 (2016) 171.
[57] S. Sadhal, R.E. Johnson, J. Fluid Mech. 126 (1983) 237.
[58] J. Cano-Lozano, P. Bohorquez, C. Martínez-Bazán, Int. J. Multiph. Flow 51 (2013) 11.
[59] R. Mei, J.F. Klausner, Phys. Fluids A 4 (1992) 63.
[60] R. Mei, J.F. Klausner, C.J. Lawrence, Phys. Fluids 6 (1994) 418.
[61] S.T. Thoroddsen, M.-J. Thoraval, K. Takehara, T.G. Etoh, J. Fluid Mech. 708 (2012) 469–479.
[62] C.-K. Gong, X. Xu, Q. Yang, Chem. Eng. J. 443 (2022) 136382.
[63] X. Yang, C. Chen, T. Zhang, X. Tian, R. Zhang, D. Manhaeghe, Y. Zhao, S. Song, K. Demeestere, S.W. Van Hulle, Chem. Eng. J. 458 (2023) 141461.
[64] K. Cui, K. Guo, J.M. Carvajal-Arroyo, J. Arends, K. Rabaey, Chem. Eng. J. 471 (2023) 144296.
[65] A. Bose, R. O'Shea, R. Lin, J.D. Murphy, Chem. Eng. J. 437 (2022) 134988.